

Design and Performance of a Thermal Neutron Imaging Facility at the North Carolina State University PULSTAR Reactor

Kaushal K. Mishra, Ayman I. Hawari, and Victor H. Gillette

Abstract—A thermal neutron imaging facility has been set up at the North Carolina State University PULSTAR reactor. The PULSTAR is an open pool light water moderated 1 MWth research reactor with six beam tubes. The present facility is set up on beam tube # 5 of the reactor. The facility is intended to have radiographic and tomographic capabilities. The design of the neutron collimator was performed using MCNP5. The collimator includes a 4-in bismuth filter followed by a 6-in single-crystal sapphire filter. Thermal neutron scattering cross-section libraries for sapphire and bismuth were generated and used in the MCNP simulation of the system. Based on the current design, the L/D of the facility ranges between 100 and 150. The neutron flux at the image plane can be varied from 1.8×10^6 to 7×10^6 n/cm²·s with a Cd-ratio of ~ 450 . The resolution of the system for different imaging media was also estimated and found to be $\sim 33 \mu\text{m}$ for conventional radiography film and $\sim 110 \mu\text{m}$ for digital image plates. Initial measurements, using ASTM standards, show that the imaging facility achieves a beam quality classification of I^A.

Index Terms—MCNP, Monte Carlo simulation, neutron beam filters, neutron collimator, neutron imaging, neutron radiography.

I. INTRODUCTION

THE use of neutrons in imaging has been on-going since the mid-20th century. The technique is characterized by the fact that the attenuation of neutrons in matter is dependent on the cross section of interaction between a neutron and the nucleus. The image contrast is formed due to this attenuation. In conventional neutron imaging, this is mainly due to the absorption and large angle scattering of the neutrons as they penetrate through the sample. Consequently, neutrons are attenuated by light materials (e.g., water, hydrocarbons, etc.) and some highly absorbing elements like boron, cadmium, and gadolinium, while they are more penetrating of heavy materials such as steel and lead. In addition, due to the nuclear nature of the interaction process, isotopic differentiation for a given element is possible with neutrons.

Radiation imaging is one of the commonly used techniques for nondestructive evaluation (NDE) of materials. Conventionally, X-rays (and γ -rays) have been used for this purpose. In comparison to neutrons, X-ray attenuation increases with electron density. In this case, materials that may appear near trans-

Manuscript received May 2, 2006; revised July 24, 2006. This work was supported by the U.S. Department of Energy under Grant DE-FG07-03ID14532.

The authors are with the Department of Nuclear Engineering, North Carolina State University, Raleigh, NC 27607 USA (e-mail: kkmishra@ncsu.edu; ayman.hawari@ncsu.edu; vhgillet@ncsu.edu).

Color versions of one or more of the figures in this paper are available online at <http://ieeexplore.ieee.org>.

Digital Object Identifier 10.1109/TNS.2006.884323

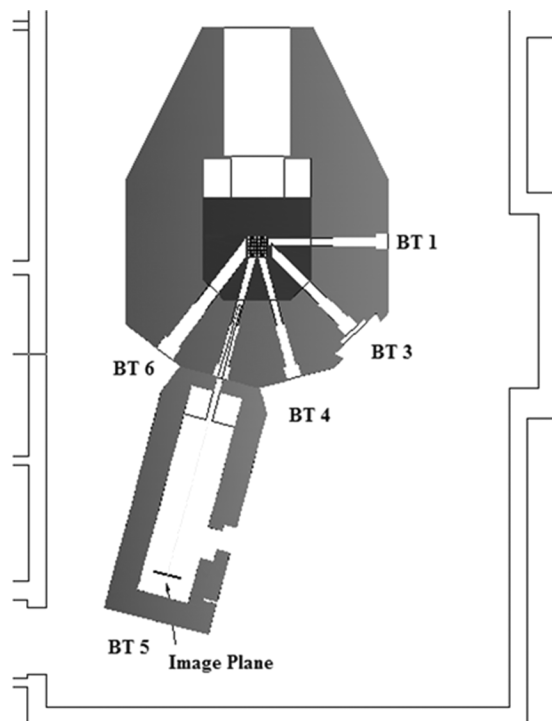


Fig. 1. A schematic of the PULSTAR reactor showing the biological shield and the beam tubes along with the neutron imaging facility on BT #5. Beam tube #2, which is the through tube, is not shown.

parent to neutrons are found to be opaque to X-rays (e.g., lead) which limits the use of X-ray imaging for high density material components. Also, for radioactive samples, film fogging is a concern when using X-rays, which is easily eliminated using neutrons. This makes neutrons more suited for applications like imaging of spent nuclear fuel pins, fuel cells, refrigeration systems, water flow path in plants, etc.

A neutron imaging facility has been set up at the North Carolina State University (NCSSU) PULSTAR reactor. The reactor is a swimming pool type 1-MWth research reactor with the core placed inside a 15 000 gallon open tank of water. Light water acts as both the coolant and moderator. The core is rectangular and has dimensions of $24 \times 15 \times 13$ inches. It is loaded with a 5×5 array of rectangular fuel assemblies. Each fuel assembly includes 25 UO₂ fuel pins enriched to 4% in U-235. To enhance the neutron economy, two sides of the core are reflected by graphite and beryllium. Six beam tubes (BT) are positioned in the pool and provide neutrons for experimental purposes. The layout of the PULSTAR reactor is shown in Fig. 1 including the arrangement of the beam tubes.

II. DESIGN CONSIDERATIONS

A. Criteria and Constraints

The neutron imaging facility at NCSU is designed to have real-time capabilities and to be usable in performing conventional radiography and tomography. Initial set up and testing have been conducted using BT #5 of the reactor (see Fig. 1). Presently, the facility can perform film and digital radiography. The development of the real-time radiography and tomography system is in progress and will be achieved in the near future.

The principal component of this facility is its neutron collimator, which is based on the commonly used divergent beam approach. In this case, a fundamental collimator design parameter is known as the L/D ratio, where D is defined as the size of the beam aperture, and L is the distance from the aperture to the image plane. The L/D ratio determines the geometric unsharpness of the obtained radiograph. Consequently, the design study has been performed to meet the following objectives: an L/D of ~ 150 , a quality I^A beam as designated by the American Society of Testing and Materials (ASTM) standards [1], a maximum neutron to gamma (N/G) ratio, a maximum thermal neutron content (TNC), and a uniform beam at the image plane of ~ 48 -cm size to accommodate large size conventional radiography film. In addition, the ability to vary these parameters to suit the application was also taken into consideration.

Furthermore, several constraints were considered during the design process. This includes a maximum available beam line length of 6 m, a reasonable thermal neutron flux at the farthest image plane ($>10^6$ n/cm²/s), and a dose rate of 1 mR/h at full power near and around the facility outside the shielding. Based on an L/D of 150 and a maximum beam line length of 6 m, the aperture size was taken to be 4 cm with a square cross section. The aperture defining material is boral. The location of the aperture relative to the beam tube entrance was calculated to be 189 cm, which defines a beam divergence angle of $\sim 2.29^\circ$.

B. Design Performance Using Simulations

The detailed collimator design (and its expected performance) was investigated using MCNP Monte Carlo simulations [2]. The simulation was carried out in two stages. In the first stage, the PULSTAR reactor core simulation was performed to obtain the neutron and gamma source energy spectrum at the beam tube entrance. The MCNP model of the reactor core is shown in Fig. 2. The obtained neutron energy spectrum at the beam tube entrance is shown in Fig. 3. Further simulations showed that the use of additional moderation to increase the fraction of thermal neutrons in the spectrum is not effective and would result in significant flux reduction. In addition, the calculations also revealed the existence of a large gamma flux in the beam. This is due to the fact that BT #5 has a direct view of the PULSTAR core.

The second stage of the simulation included the transport of the neutron and gamma radiation incident on BT #5 entrance, through the collimator up to the image plane. To achieve the design objectives stated above, the first aspects studied were the filter requirements. For this purpose, the incident neutron spectrum was transported to the image plane without using any filter

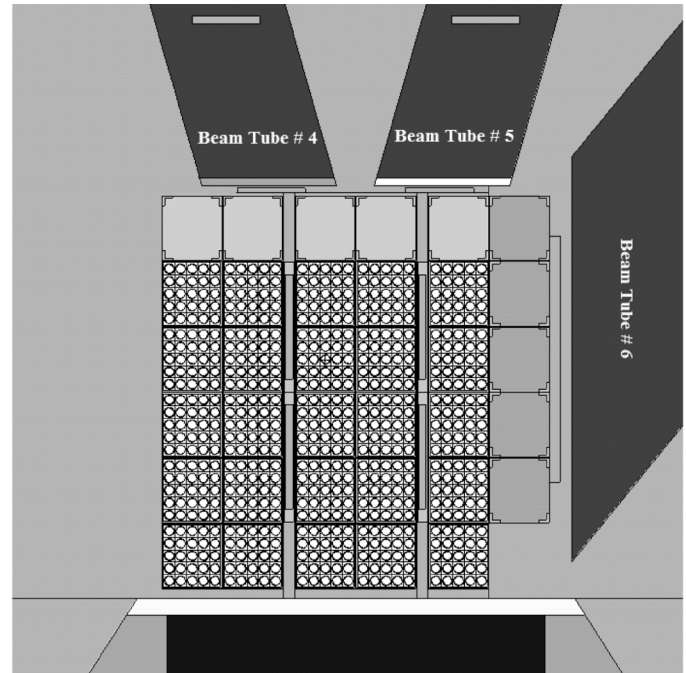


Fig. 2. The MCNP model of the reactor core simulated to obtain the neutron and gamma energy spectra at the entrance of beam tube #5.

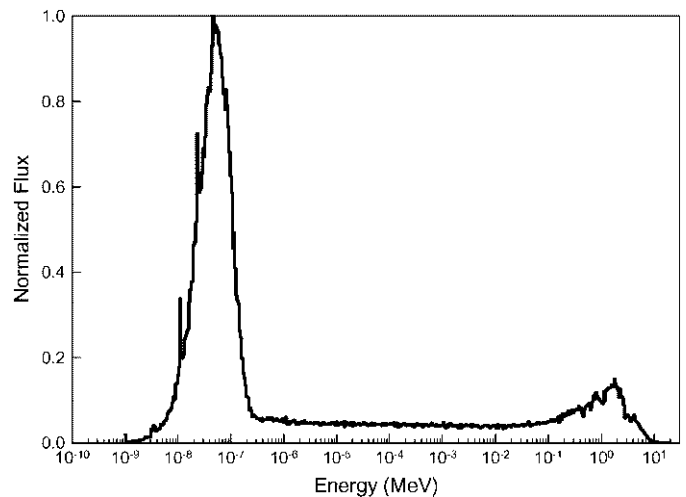


Fig. 3. The simulated neutron energy spectrum ($d\phi/d(\ln(E))$) at the entrance of BT #5 closest to the core.

in the collimator. The predicted neutron spectrum at the image plane is shown in Fig. 4. This demonstrated the fact that the neutron beam in this case will have significant fast neutron content. Also, the fast neutron content increased in the transport through the collimator because of comparatively more absorption of thermal neutrons inside the collimator. Consequently, to meet the objectives of a high N/G ratio and a high TNC, the use of neutron and gamma filters was deemed necessary. The possible choices considered for this purpose included silicon, quartz, sapphire, bismuth, and lead. A 2.5-in diameter single crystal sapphire was selected as a fast neutron filter due to its proven quality as a filter at room temperature as opposed to cryogenically cooled silicon and quartz [3], [4]. Also, the transmission characteristics of sapphire are not expected to be altered

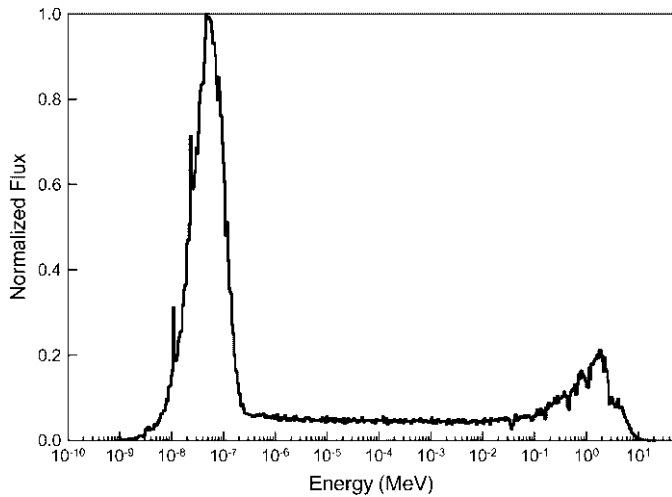


Fig. 4. The simulated neutron energy spectrum ($d\phi/d(\ln(E))$) at the 6-m image plane without using filters.

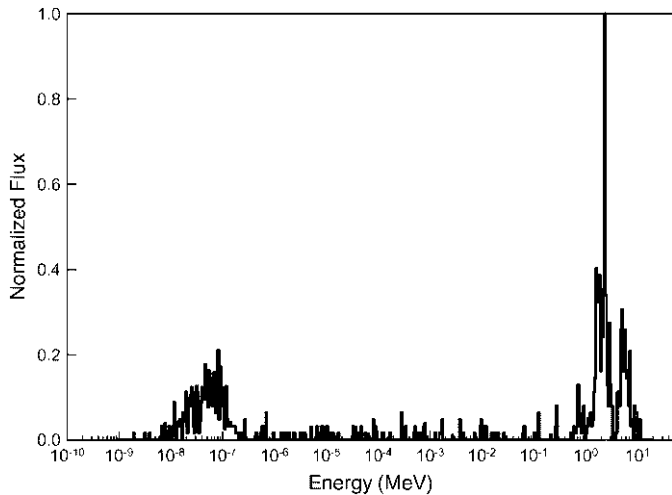


Fig. 5. The simulated neutron energy spectrum ($d\phi/d(\ln(E))$) at the 6-m image plane through 4-in Bi and 6-in sapphire filters and using free atom cross sections.

even after years of exposure in the neutron beam. For gamma filtration, a 2.5-in diameter bismuth poly-crystal was chosen.

After including the bismuth and sapphire filters in the collimator, the neutron spectrum was again transported to the image plane. The free atom cross-section libraries that are supplied with the MCNP code were used in the calculation. In this case, the obtained spectrum did not show the effect of fast neutron filtering. Fig. 5 shows this spectrum. This result demonstrated that an accurate design simulation (capturing filtration effects) requires the use of the appropriate thermal neutron scattering cross sections.

The preparation of the thermal neutron scattering cross section libraries for both bismuth and sapphire was performed using the NJOY code system and its associated LEAPR module [5], [6]. LEAPR calculates the scattering law for a given material using the incoherent approximation. The outcome of the LEAPR calculation is processed using the THERMR module to calculate the cross sections. Finally, the ACER module is

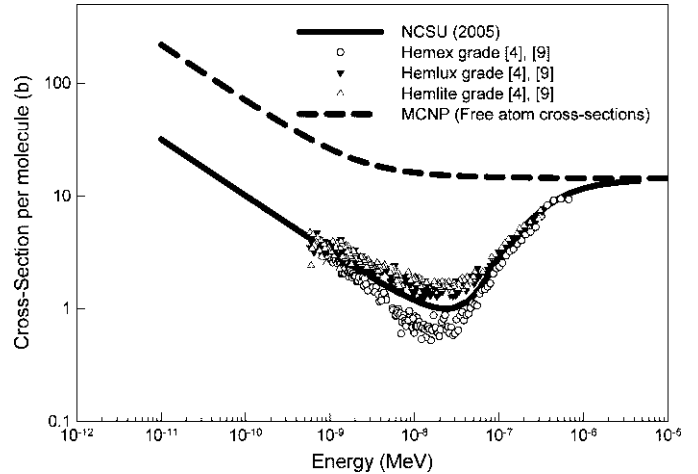


Fig. 6. The calculated single crystal sapphire thermal neutron total cross sections and comparison with experimental data. Hemex, Hemlux, and Hemlite are three grades of sapphire mainly differing in the degree of crystal alignment and the photon transparency. The experimental data are shown as symbols, while the computational data are shown as solid and dashed lines.

used to produce cross section libraries in the ACE (continuous energy) format that is utilized by MCNP.

For crystalline materials, the fundamental input for the LEAPR calculation are the vibrational (i.e., phonon) spectra of the atoms in the material. The phonon spectra used in this work were obtained by performing a crystal dynamic calculation using the PHONON code [7]. This code uses the direct method and the harmonic approximation to perform such analysis. The interatomic force information that are required by PHONON were calculated using the ab initio code VASP [8], which applies density functional theory to perform its analysis. The details of the PHONON/VASP calculations are given elsewhere [9]. For both sapphire and bismuth, Bragg scattering of low energy neutrons was neglected. This assumption is generally valid for single crystals that are preferentially oriented relative to the neutron beam. In this paper, a single crystal of sapphire filter [4] and a bismuth filter with large poly-crystals are used. The calculated total thermal neutron cross sections for single crystal sapphire and bismuth are shown in Figs. 6 and 7, respectively. From the figures, the large difference between the calculated and the free-atom cross sections can be clearly observed. The calculated cross sections were verified by comparison with the published experimental data [10]–[13], which are also shown in the figures. The neutron energy spectrum at the image plane obtained using the generated cross-section libraries for sapphire and bismuth single crystals is shown in Fig. 8. From the figure, it can be clearly observed that the fast neutron flux has been filtered out and the beam consists mainly of the desired thermal neutrons. The gamma content in the beam was also reduced significantly by the use of the 4 in of bismuth. The final MCNP collimator design model is shown in Fig. 9.

C. Design Verification Using Simulations

The design of the collimator was verified against the design objectives using MCNP simulations. A beam uniformity simulation was conducted using the designed collimator. The obtained neutron flux spatial distribution at the image plane is

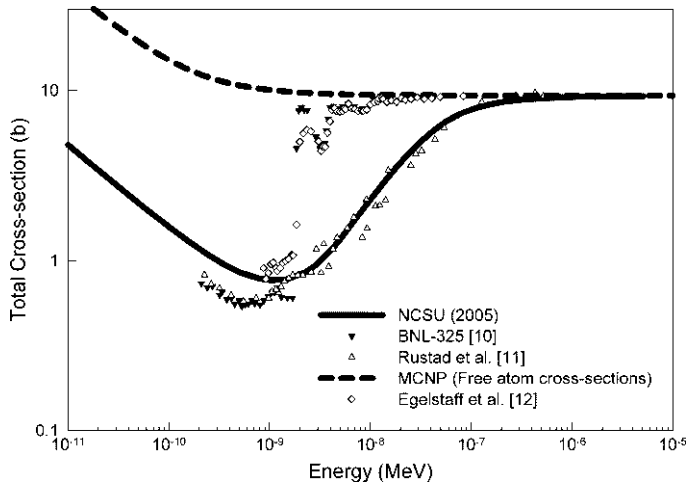


Fig. 7. The calculated single crystal bismuth thermal neutron total cross sections and comparison with experimental data. The experimental data are shown as symbols, while the computational data are shown as solid and dashed lines.

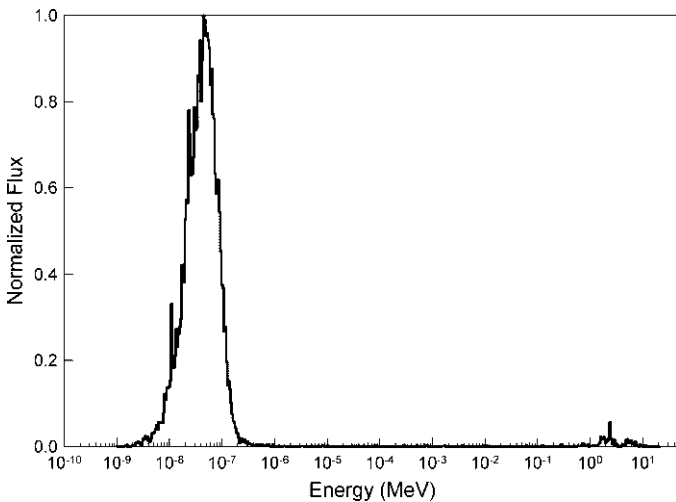


Fig. 8. The simulated neutron energy spectrum ($d\phi/d(\ln(E))$) at the 6 m image plane with 4-in Bi and 6-in sapphire filters using the generated thermal neutron scattering cross sections.

shown in Fig. 10. It clearly indicates that the flux is uniform over a length of 40 cm. A simulation of the ASTM Beam Purity Indicator (BPI) was also performed. The obtained radiograph is shown in Fig. 11 and the calculated parameters are listed in Table I. From the predicted parameters it can be concluded that the beam as designed is anticipated to meet ASTM I^A quality standards. Table I also gives the final parameters for the designed thermal neutron imaging facility.

In addition, the expected resolution performance, using the designed collimator, for radiography film, image plate (IP) systems, and scintillation screens with CCD imaging media was estimated by including the various components that contribute to the resolution in the simulation. Specifically, the geometric unsharpness, the recorder resolution and the grid resolution effects were taken into account. For the geometric unsharpness, an L/D of 150 with an object to image plane distance of 2.5 mm (typical thickness of the recorder holding cassette) was considered. The recorder resolution of radiography film, image plates,

and scintillation screens was taken as 20, 93, and 100 μm , respectively, [14]–[16]. This component was included in the simulation by estimating an effective object to image plane distance that would result in a combined resolution that is equivalent to the linear sum of the recorder resolution and the geometric resolution [17], [18]. Finally, the grid resolution effect was modeled by adjusting the pixel size that is used in the simulation. The grid resolution for the digitization of film, the IP scanning system and the CCD were taken as 25, 50, and 25 μm , respectively. The resulting PSF distributions are shown in Fig. 12. The sharp edges in the PSF appear due to the grid discretization process considered in the calculation. The resolution for the various systems, as quantified by the FWHM of the PSF, are ~ 35 , ~ 105 , and ~ 115 μm , respectively, for film, IP and CCD systems.

III. FACILITY CONSTRUCTION AND EXPERIMENTAL CHARACTERIZATION

The mechanical design and fabrication of the neutron collimator was performed in a modular fashion. This eases the modification of beam characteristics by changing beam filter length, incorporating cooling mechanisms and changing aperture size without requiring the change of the entire collimator. In addition to the collimator, other components of the imaging facility include the beam shutter, the shielding enclosure, and the detection system. The beam shutter has a rotating drum type design, which is opened by an air cylinder. The closing of the shutter is gravity controlled, which provides passive safety. The shielding enclosure of the beam shutter has walls that include a 0.25-in-thick boral plate, 6 in of lead followed by ~ 19 inches of RX-277 (concrete type material with 1.6% boron content). The shield has been designed to be made up of poured concrete in steel moulds.

Preliminary characterization of the facility was performed after inserting the collimator in the beam tube. Neutron flux measurements were performed using gold foil activation. The measured flux was approximately $2.5 \times 10^{12} \pm 10\%$ n/cm²·s with a cadmium ratio of ~ 90 at the entrance of BT #5 and approximately $1.8 \times 10^6 \pm 6\%$ n/cm²·s with a Cd ratio of ~ 450 at the 6-m image plane. The beam uniformity test was also performed and the profile is shown in Fig. 13. The result indicated a uniform beam profile with a standard deviation of $\pm 1.0\%$ which is considered consistent with the design objective.

ASTM standard E545 was followed to determine the quality of the beam [1]. Both the BPI test (see Fig. 11) and the Sensitivity Indicator (SI) tests were performed. According to these tests an I^A beam quality was achieved. Table II presents the parameters of the beam as defined by the ASTM standard using conventional radiography film. The variation in the densitometer readings for the radiographs used to obtain the ASTM parameters was within $\pm 3.5\%$ of the mean of five measurements taken across the film, which is less than the $\pm 5.0\%$ limit prescribed in E545. The table also contains the data measured using digital image plates. The variation in the readings obtained from the image plate was $\sim \pm 5\%$. The values obtained using image plates are comparable with those obtained using film except that the number of visible holes in the radiograph of the SI is only 4 which constitute the first row of the holes in the SI. This is attributed to the fact that

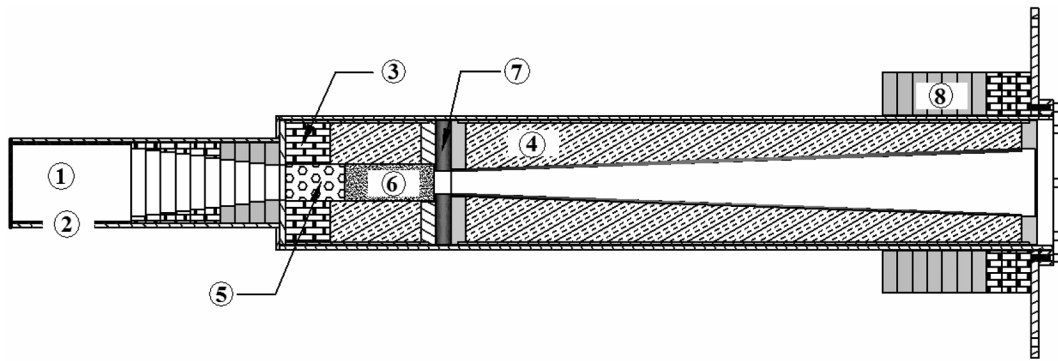


Fig. 9. The collimator model used in the MCNP simulation. The various components that are shown in the figure are: (1) air, (2) aluminum, (3) lead, (4) RX-277 (concrete-type material with 1.6% boron content), (5) bismuth filter, (6) sapphire filter, (7) boral, and (8) borated polyethylene.

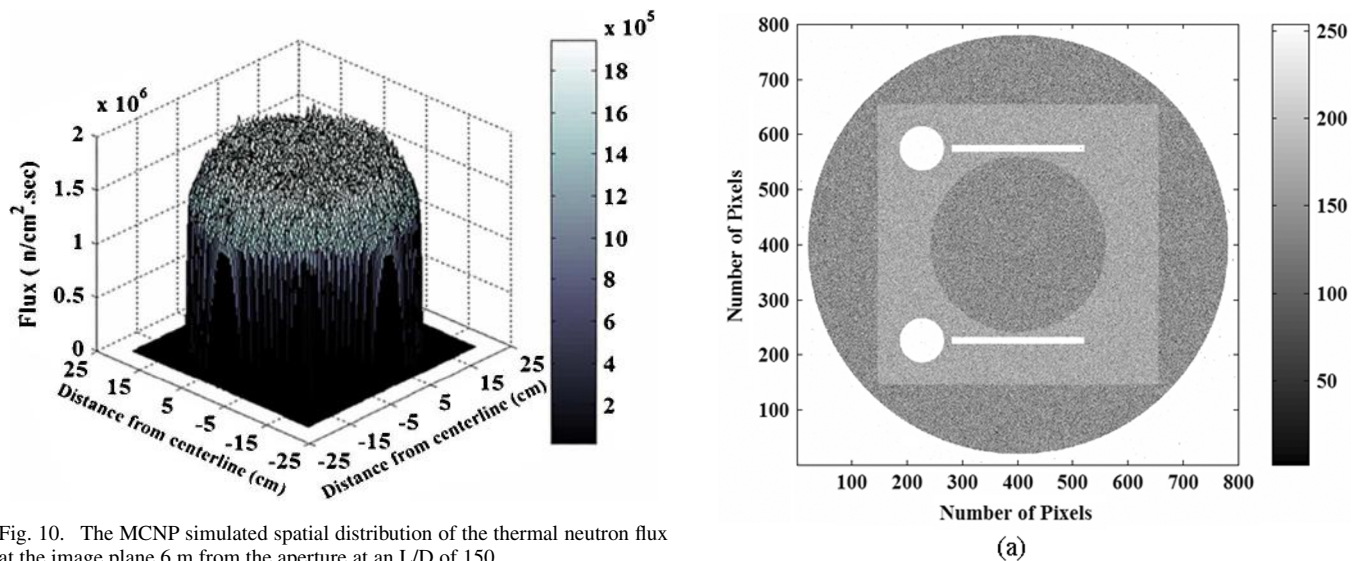


Fig. 10. The MCNP simulated spatial distribution of the thermal neutron flux at the image plane 6 m from the aperture at an L/D of 150.

image plates have less spatial resolution than film. In addition, the gamma and pair production contents obtained using image plates are much less than film. This is attributed to their reduced gamma sensitivity. The uncertainties in the parameters given in Table II are estimated using the variation in the readings of the film and image plates that are reported earlier and propagating this variation through the calculation.

To investigate the resolution of the system, measurements were performed of the edge spread function obtained using a 50- μm -thick gadolinium foil for both radiographic film and digital image plates. Subsequently, the line spread function (LSF) was obtained by differentiating the measured edge spread function. Fig. 14 shows the film LSF. In this case, the experimental data were fitted using a Lorentzian spread functions [18], [19]. The film resolution (as defined by the full width at half maximum, FWHM, of the LSF) is obtained from the fit and found to be in the range of 33 μm . In the case of the LSF obtained using the IP, a Gaussian function was used to fit the LSF. Fig. 15 shows the result of this analysis, which in the IP case is consistent with the observation that a Gaussian function is more suitable. This has been attributed to the fact that the laser involved in the readout process associated with the IP has a Gaussian spread that provides extra width to the LSF [20]. The image plate resolution is found to be in the range of 110 μm . The spatial res-

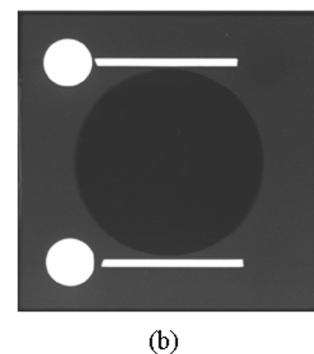


Fig. 11. (a) The MCNP simulated radiograph of the BPI. The pixel resolution is 50 μm . (b) The BPI radiograph obtained using photographic film.

TABLE I
FINAL PARAMETERS OF THE DESIGNED THERMAL NEUTRON IMAGING FACILITY

Parameter	Value
Neutron Flux	1.8×10^6 to 7×10^6 n/cm ² ·s
TNC	~70%
N/G	4.43×10^4 to 1.34×10^6 cm ² mR ⁻¹
L/D	100 to 150
Divergence	~2.29°
Cd Ratio	~450
Scatter content	~1.8%

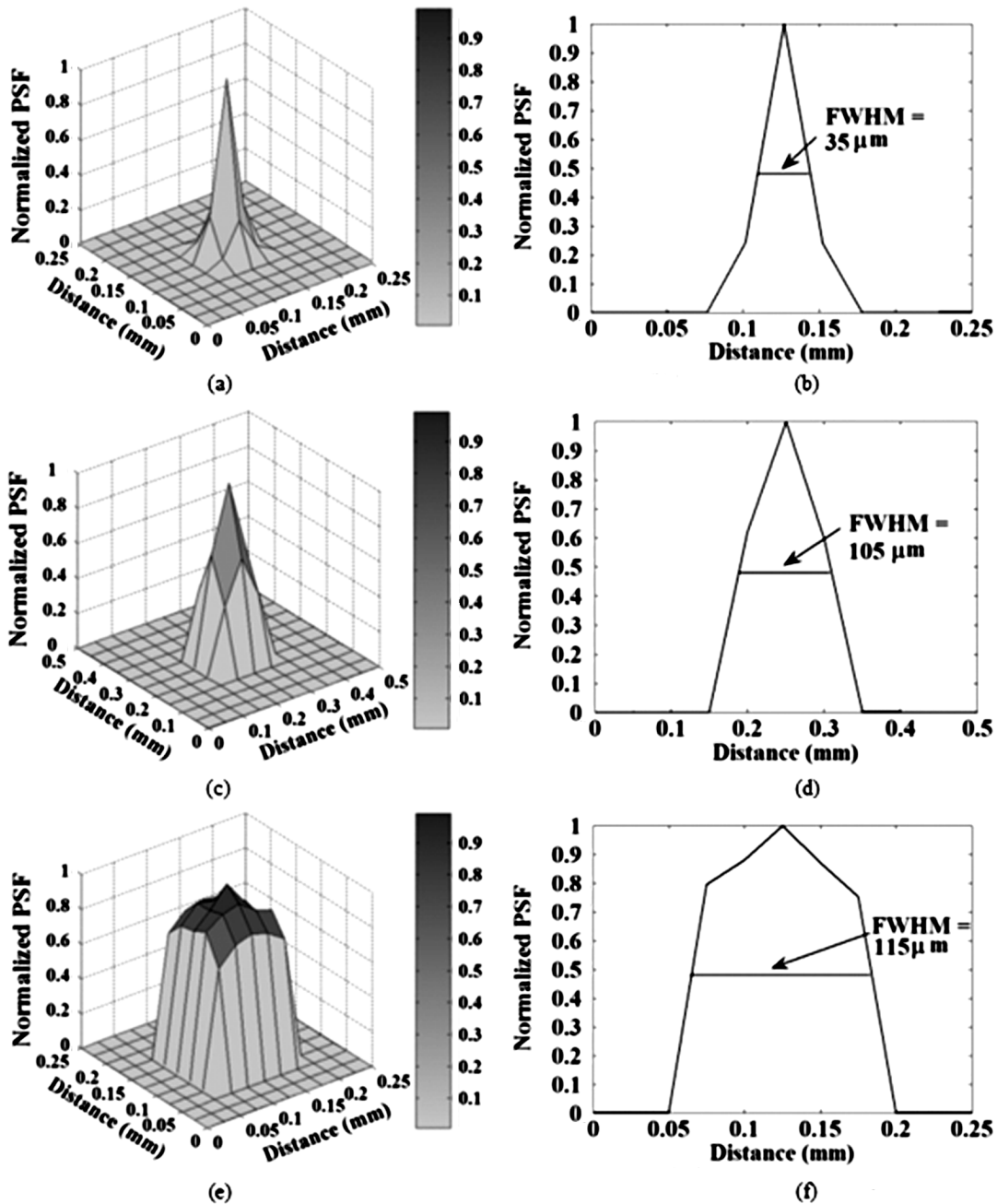


Fig. 12. The simulated PSF for different imaging media. (a) Film PSF. (b) Vertical slice of film PSF. (c) Image plate PSF. (d) Vertical slice of image plate PSF. (e) Real-time system PSF. (f) Vertical slice of real-time system PSF.

olution estimates obtained from the curve fittings for the film and image plate are within the resolution ranges published for these detection systems [14]. The difference in resolution between film and IP is due to the larger recorder resolution of the digital image plates, which is known to be $\sim 93 \mu\text{m}$ as opposed to the $\sim 20 \mu\text{m}$ recorder resolution of conventional radiography film [15].

Finally, it can be seen that good agreement exists between the resolution estimates that are obtained from measurement and simulation. This verifies the assumptions made in the simulation including the expected behavior of the neutron collimation system as designed and implemented. Consequently, the models developed in this paper will be valuable for exploring further

developments of this facility. A comparison of the developed NCSU neutron imaging facility with selected other facilities is given in Table III.

IV. CONCLUSION

A thermal neutron imaging facility has been set up at the NCSU PULSTAR reactor. The design of the facility was performed using the MCNP Monte Carlo code. Preliminary characterization of the facility shows a thermal neutron flux of $\sim 1.8 \times 10^6 \text{ n/cm}^2 \cdot \text{s}$ with a Cd ratio of ~ 450 at the 6 m image plane. Furthermore, the resulting thermal beam was characterized using the ASTM BPI and SI indicators and was found to have the characteristics of a I^A beam. Currently, work is on going to establish

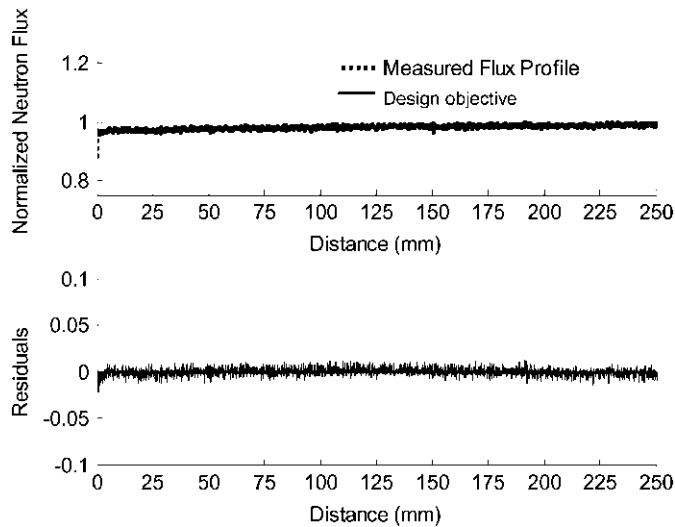


Fig. 13. The measured neutron beam profile (as a function of the distance across the image plate). The measurement was performed at the image plane at a 6 m distance from the aperture.

TABLE II
MEASURED BEAM PARAMETERS ACCORDING TO ASTM E545 STANDARD

ASTM Parameters	Conventional film	Digital Image Plate
Effective TNC	73.45 ± 3.5%	77.58 ± 5.0%
Scatter content	2.41 ± 3.5%	1.96 ± 5.0%
Gamma content	0.69 ± 5.0%	0.19 ± 7.1%
Pair production content	1.72 ± 3.5%	0.38 ± 5.0%
Holes visible	7	4
Gaps visible	7	7

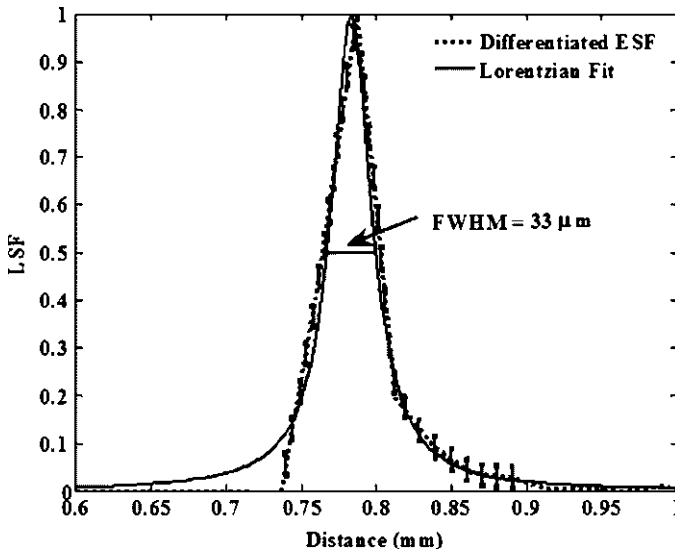


Fig. 14. The measured LSF using conventional radiography film. The data were fit to a Lorentzian function and the FWHM was extracted from the fit results.

real-time radiography and computed tomography capabilities at the facility.

ACKNOWLEDGMENT

The authors would like to acknowledge the helpful discussions with Dr. D. Jacobson and Dr. M. Arif of the National In-

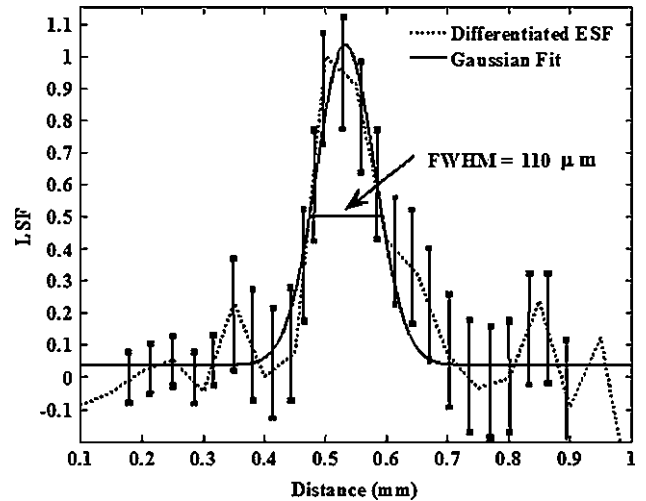


Fig. 15. The measured LSF using digital image plates. The data were fit to a Gaussian function and the FWHM was extracted from the fit results.

TABLE III
A COMPARISON OF THE NCSU NEUTRON IMAGING FACILITY WITH OTHER FACILITIES

Imaging Facility	Neutron Source	Neutron Flux (n/cm ² sec)	Beam Filters	L/D
NCSU	1MWth Reactor (flux ~2.5x10 ¹² n/cm ² sec)	1.8x10 ⁶ to 7x10 ⁶	4 inch bismuth and 6 inch sapphire	100 to 150
National Institute of Standards and Technology (NIST) [21]	20 MWth Reactor (flux ~4x10 ¹⁴ n/cm ² .sec)	4.75x10 ⁶ to 1.84x10 ⁷	10 cm bismuth	280 to 560
Paul Scherrer Institute (PSI) [22]	Spallation Source (flux ~10 ¹⁴ n/cm ² /sec)	3.96x10 ⁶ to 2.82x10 ⁷	5 cm bismuth	200 to 550

stitute of Standards and Technology (NIST) during the initiation of this project. The help of A. Cook and the staff of the NCSU PULSTAR reactor in the set up of this facility is highly appreciated.

REFERENCES

- [1] Metals test methods and analytical procedures vol. 03.03, sec. 3, 1999, Ann. Book of ASTM Stand., Nondestructive Testing.
- [2] X-5 Monte Carlo Team, MCNP—A General Monte Carlo N-Particle Transport Code, Version 5 Los Alamos Nat. Lab., Los Alamos, NM, Tech. Rep. LA-UR-03-1987, 2003.
- [3] D. C. Tennant, "Performance of a cooled sapphire and beryllium assembly for filtering of thermal neutrons," *Rev. Sci. Instrum.*, vol. 59, pp. 380–381, 1988.
- [4] D. F. R. Mildner, M. Arif, and C. A. Stone, "Neutron transmission of single crystal sapphire filters," *J. Appl. Crystallogr.*, vol. 26, pp. 438–447, 1993.
- [5] R. E. MacFarlane and D. W. Muir, The NJOY nuclear data processing system, Version 91 Los Alamos Nat. Lab., LA-12740-MS, 1994.
- [6] R. E. MacFarlane and D. W. Muir, New thermal neutron scattering files for ENDF/B-VI, Release 2 Los Alamos Nat. Lab., LA-12639-MS, 1994.
- [7] K. Parlinski, *PHONON Manual, Version 3.11*. Cracow, Poland: Institute of Nuclear Physics, 2002.
- [8] G. Kresse and J. Furthmuller, *Vienna Ab-Initio Simulation Package; VASP the Guide*. Vienna: Austria, 2002.

- [9] A. I. Hawari, I. I. Al-Qasir, and K. K. Mishra, "Accurate simulation of thermal neutron filter effects in the design of research reactor beam applications," in *PHYSOR-2006: Advances in Nuclear Analysis and Simulation*, Vancouver, Canada, 2006.
- [10] A. K. Freund, "Cross-sections of materials used as neutron monochromators and filters," *Nucl. Instrum. Methods Phys. Res.*, vol. 213, pp. 495–501, 1983.
- [11] D. J. Hughes and J. A. Harvey, *Neutron Cross Sections* (in Brookhaven Nat. Lab. Rep. 325, Office Tech. Services, Dep. Commerce). Wash., D.C.: , 1955.
- [12] B. M. Rustad, J. Als-Nielsen, A. Bahnsen, C. J. Christensen, and A. Nielsen, "Single-crystal filters for attenuating epithermal neutrons and gamma rays in reactor beams," *Rev. Sci. Instrum.*, vol. 36, pp. 48–54, 1965.
- [13] P. A. Egelstaff and R. S. Pease, "The design of cold neutron filters," *J. Sci. Instrum.*, vol. 31, pp. 207–212, 1954.
- [14] E. H. Lehmann, P. Vontobel, G. Frei, and C. Brönnimann, "Neutron imaging-detector options and practical results," *Nucl. Instrum. Methods Phys. Res. A*, vol. 531, pp. 228–237, 2004.
- [15] H. Kolbe, E. Lehmann, W. Gunia, and S. Korner, "Applications and characteristics of imaging plates as detectors in neutron radiography at SINQ," *Nucl. Instrum. Methods Phys. Res. A*, vol. 424, pp. 40–47, 1999.
- [16] R. Baker, Applied Scintillation Technologies. Annapolis, MD, Jun. 2005, private communication.
- [17] A. Bouwers, *Fortschr. Geb. Röntgenstrahl.*, vol. 54, p. 87, 1936.
- [18] A. A. Harms and A. Zeilinger, "A new formulation of total unsharpness in radiography," *Phys. Med. Biol.*, vol. 22, no. 1, pp. 70–80, 1977.
- [19] A. A. Harms, B. K. Garside, and P. S. W. Chan, "Edge-spread function in neutron radiography," *J. Appl. Phys.*, vol. 43, pp. 3863–3867, 1972.
- [20] J. Hofmann and C. Rausch, "Performance of a prototype detector system for thermal neutron based on laser stimulated luminescence," *Nucl. Instrum. Methods Phys. Res. A*, vol. 355, pp. 494–500, 1994.
- [21] D. S. Hussey, D. L. Jacobson, M. Arif, P. R. Huffman, R. E. Williams, and J. C. Cook, "New neutron imaging facility at NIST," *Nucl. Instrum. Methods Phys. Res. A*, vol. 542, pp. 9–15, 2005.
- [22] E. Lehmann, H. Pleinert, and L. Wiesel, "Design of a neutron radiography facility at the spallation source SINQ," *Nucl. Instrum. Methods Phys. Res. A*, vol. 377, pp. 11–15, 1996.